Dalton Transactions

ROYAL SOCIETY OF CHEMISTRY

PAPER

View Article Online
View Journal | View Issue

Cite this: *Dalton Trans.*, 2026, **55**, 894

Boosting oxygen evolution reaction performance *via* hydrothermally synthesized 4A zeolite-supported Ni catalysts: structure–activity relationship investigation

Xiuzhen Xie, *[a,b] Chenglu Hu,[a,c] Cao Luo,[a] QiuJie Shi,[a] Yongyang Wang,[a] Zhuohan Xie,[a] Zihan Yao,[a] Qizhi Le[a,c] and Wen-yi Hu*[a]

Received 11th October 2025,
Accepted 10th December 2025

DOI: 10.1039/d5dt02450a

rsc.li/dalton

The development of efficient and stable electrocatalysts for the oxygen evolution reaction (OER) is crucial for renewable energy conversion and storage systems. In this study, a series of 4A zeolite-supported Ni (4A/*x*Ni, *x* = 20, 40, 60, 80 wt%) materials were synthesized *via* a facile hydrothermal method. The physicochemical properties of the 4A/*x*Ni materials were thoroughly characterized using powder X-ray diffraction (PXRD), transmission electron microscopy (TEM), Fourier transform infrared spectroscopy (FTIR), Brunauer–Emmett–Teller method (BET), X-ray photoelectron spectroscopy (XPS), scanning electron microscopy (SEM), energy dispersive X-ray spectroscopy (EDS), inductively coupled plasma analysis (ICP), and electrochemical tests. The specific surface area of the 4A/80 wt% Ni product was approximately 25 times greater than that of the pristine 4A zeolite. The electrochemical performance of these materials was evaluated using linear sweep voltammetry (LSV). The 4A/60 wt% Ni sample exhibited superior catalytic activity, with low onset potential (1.389 V *vs.* RHE), low Tafel slope (19 mV dec^{-1}), and low ohmic resistance (157 Ω) compared to the 4A zeolite. Moreover, the largest capacitance density (C_{dl}) of 98.3 μF cm^{-2} was recorded for 4A/60 wt% Ni, indicating its high electrochemical active surface area. These results demonstrate that the as-prepared 4A/*x*Ni (*x* = 20, 40, 60, 80 wt%) materials are promising electrodes for OER applications, showcasing their potential as efficient and durable catalysts for electrochemical water splitting.

1 Introduction

Zeolites, a class of aluminosilicate minerals with microporous structures, are widely studied for applications in catalysis, adsorption, and separation. Among them, 4A zeolite has attracted significant attention in catalysis owing to its high thermal stability and specific ion-exchange capacity.[1] In practice, most heterogeneous catalysts contain one or more catalytically active compounds supported on a substrate. For zeolite-supported catalysts, active transition metals are incorporated *via* ion exchange and subsequent processing, yielding materials with tailored porous, chemical, and electronic properties.

Zeolite-supported metal catalysts are classified into three types based on the source and location of metal species within the zeolite channels. (1) Catalysts with metal atoms incorporated as heteroatoms in the zeolite framework, which migrate into the zeolite pores through thermal treatment or reduction.[2,3] (2) Catalysts with metal species (*e.g.*, Pt, Pd, Ni) that cannot integrate into the framework but remain in micropores, eventually forming encapsulated metals or metal oxides upon calcination or reduction.[4–6] (3) Catalysts with metal species encapsulated in intra-crystalline mesopores; during zeolite crystallization, the metal cations stabilize the framework, enabling *in situ* encapsulation within micropores.[7–9]

Under high-temperature conditions, nickel nanoparticles undergo migration and agglomeration, resulting in a significant decrease in specific surface area. Consequently, the number of catalytic active sites is reduced, deteriorating the catalyst performance. This effect is more pronounced in high-temperature reactions, such as methane reforming.[10] Ni-based catalysts synthesized by the conventional impregnation method, without modifying or treating the mesoporous structure or surface of the zeolite support, are prone to Ni particle

[a]*College of Chemistry and Material Science, Longyan University, Longyan 364012, Fujian Province, People's Republic of China. E-mail: xiexiuzhen@lyun.edu.cn*
[b]*Department of Materials Science and Engineering, College of Materials, Xiamen University, No. 422 Siming South Road, Xiamen, 361005, Fujian Province, China*
[c]*Key Lab of Electromagnetic Processing of Materials, Ministry of Education, Northeastern University, Shenyang, People's Republic of China*

agglomeration at high temperatures. Owing to the confinement effect of zeolite micropores, encapsulated metals or metal oxides exhibit small sizes, even at the sub-nanometer or atomic scale. However, strong metal-framework interactions complicate the geometric and electronic properties of confined metal particles, making their identification challenging. The microporous channels of conventional zeolites significantly restrict the diffusion of reactants and products. In contrast, mesoporous molecular sieves with crystalline frameworks and hierarchical porosity have emerged as promising alternatives, overcoming the limited mass transfer of traditional zeolites. These hierarchically porous architectures possess high specific surface areas and large pore volumes, facilitating the effective dispersion of transition metal ions or noble metal species within the zeolitic structure.[11] For example, Ni–H beta zeolite exhibited excellent performance in the electrocatalytic oxidation of methanol,[12,13] and CeO_2-modified nano-ZSM-5 also showed remarkable activity in the electrochemical oxidation of methanol.[14] However, current zeolite-based catalysts generally require multi-step synthesis procedures, which are labor-intensive and time-consuming.[14,15]

Herein, 4A zeolite-supported nickel (4A/*x*Ni) catalysts are synthesized *via* a facile hydrothermal method to enhance the surface area and active site density, addressing these limitations. The as-prepared 4A/Ni materials are demonstrated to be promising electrode materials for oxygen evolution reaction (OER) applications. This work reveals the correlation between Ni loading, specific surface area, and OER activity in 4A/*x*Ni, and provides new insights into the design of zeolite-based OER catalysts.

2 Experimental section

2.1 Methods

2.1.1 Preparation of 4A zeolite. First, kaolin was activated with an alkaline solution and used as the raw material for 4A zeolite preparation. The specific process is as follows. A mixture of 0.10 g kaolin (containing 44.03 wt% SiO_2 (0.734 mmol), 40.98 wt% Al_2O_3 (0.402 mmol)), and 10 mL of 6 M NaOH was placed in a closed Teflon-lined stainless-steel autoclave. The autoclave was then heated in an oven at 200 °C for 4 hours. After crystallization, the product was centrifuged and washed with deionized water three times. The solid was separated and dried at 75 °C for 24 hours to obtain ~0.1 g of activated kaolin, which was used as the subsequent raw material.[16,17]

Next, 2.5 g of activated kaolin and 6 mL of HCl were mixed into 20 mL of deionized water with stirring. Then, 10 mL of 6 mol L^{-1} NaOH solution was added to adjust the pH to 14, followed by an additional 80 mL of 0.67 mol L^{-1} NaOH solution. The resulting mixture was stirred uniformly and transferred to a sealed Teflon-lined stainless-steel autoclave for hydrothermal treatment at 90 °C for 48 hours. After the reaction, the 4A zeolite product was obtained by centrifugal washing and drying, and characterized by PXRD.

2.1.2 Preparation of 4A/Ni composite. Ammonia water pretreatment (4AP) was first performed to modify the surface of 4A zeolite, which facilitates the adsorption of Ni^{2+} and its subsequent encapsulation during the hydrothermal reaction. First, 0.5 g of 4A zeolite was mixed with 5 mL of deionized water and 5 mL of $NH_3{\cdot}H_2O$, and stirred for 0.5 h. The mixture was then transferred to a closed Teflon-lined stainless-steel autoclave and heated at 120 °C for 4 h. After crystallization, the product was collected by centrifugation, washed thoroughly, and dried to obtain a white solid powder (4A-protonated, 4AP (~0.48 g)). Subsequently, 4AP (~0.48 g) was mixed with Ni $(NO_3)_2{\cdot}6H_2O$ (20, 40, 60, 80 wt%) and 10 mL of deionized water, and stirred for 1 h. The resulting solution was poured into a Teflon-lined hydrothermal reactor.

2.2 Material

Chemical reagents used in sample synthesis are shown in Table 1.

2.3 Material characterization

X-ray diffraction (XRD) measurements were performed to analyze the crystal structure of the materials using a Philips X'Pert PRO diffractometer with Cu-Kα radiation (λ = 1.54178 Å). Morphology and composition were analyzed using a scanning electron microscope (S-3400N) equipped with an energy-dispersive X-ray spectromete. Fourier transform infrared spectroscopy was carried out using an IS10 spectrometer with a spectral resolution of 2 cm^{-1} over the range of 400–4000 cm^{-1} to characterize the chemical bonds of the products. Thermogravimetric analysis was performed using a STA449F3 instrument (Nexi STA, Germany) to evaluate thermal stability, with the following test conditions: the sample was heated from 30 °C to 1000 °C in air at a heating rate of 10 °C min^{-1}. Oxygen evolution reaction (OER) performance was evaluated on a CHI660B electrochemical workstation (Shanghai CHI Instruments). The specific surface area and pore size of the samples were analyzed using the Brunauer–Emmett–Teller method (under a relative pressure (P/P_0) range of 0.0–1.0) and Barrett–Joyner–Halenda method, respectively. X-ray photo-

Table 1 Chemical reagents used in sample synthesis

Chemicals	Manufacturers	Chemicals	Manufacturers
Kaolin	Xiamen Xinysheng Non-metallic Materials Technology Co., Ltd	$Ni(NO_3)_2{\cdot}6H_2O$	Guoxiu Chemical Reagent Co., Ltd
NaOH	Guoxiu Chemical Reagent Co., Ltd	Nickel foam	Guoxiu Chemical Reagent Co., Ltd
HCl	Guoxiu Chemical Reagent Co., Ltd	$NH_3{\cdot}H_2O$	Guoxiu Chemical Reagent Co., Ltd

electron spectroscopy (XPS) was performed using an ESCALAB 250Xi spectrometer to investigate the surface elemental composition of the samples. Cyclic voltammetry (CV), electrochemical impedance spectroscopy (EIS), and constant current charge–discharge measurements were conducted using a CHI660B workstation (Chunhua Instrument).

2.3 Electrode preparation

First, nickel foam was pretreated with ethanol and acetone, thoroughly rinsed with deionized water, and finally dried for use. Then, 4AP, $Ni(NO_3)_2{\cdot}6H_2O$ (20, 40, 60, 80 wt%), and 10 mL of deionized water were magnetically stirred for an extended period until a suspension was formed. The suspension, along with the pre-cleaned nickel foam, was transferred to a 20 mL Teflon-lined oven and heated at 120 °C for 15 h. After the reactor cooled to room temperature, the nickel foam loaded with 4A zeolite-supported *x*Ni (x = 20, 40, 60, 80 wt%) was thoroughly washed with deionized water and dried to obtain the working electrode. The as-prepared samples were subjected to XRD tests to confirm their structure.

Electrochemical performance was evaluated using a three-electrode system with a saturated calomel electrode (SCE) as the reference electrode, a platinum electrode as the counter electrode, and 6 M KOH as the alkaline electrolyte. The working electrode was prepared by hydraulically pressing the catalyst slurry (containing ~5–8 mg of 4A zeolite-supported *x*Ni (x = 20, 40, 60, 80 wt%)) onto a 1 cm^2 nickel foam collector, followed by vacuum drying at 90 °C overnight. CV, EIS, and constant current charge–discharge measurements were performed using a CHI660B electrochemical workstation (Chunhua Instrument) to assess the OER performance of the 4A zeolite-supported *x*Ni electrodes. The electrochemical workstation employed in this manuscript is equipped with an *iR* compensation function, which was enabled during all electrochemical measurements to eliminate the influence of solution resistance. For the OER and EIS tests, the measurements were performed over the frequency range of 100 kHz to 1 Hz with an AC perturbation amplitude of 5 mV, and the applied DC bias was set to the open-circuit voltage (OCV) of the system. The EIS data were fitted using ZSimpWin software, and a rotating electrode was adopted to mitigate bubble accumulation and blockage at the electrode surface under high-current conditions. All tests were conducted in a 6 M KOH electrolyte solution, and the initial estimate of the charge transfer resistance (R_{ct}) for Ni-based catalysts in this system was approximately 300 Ω (corresponding to the equivalent circuit model R_s (R_{ct} CPE)).

Linear sweep voltammetry (LSV) curves were recorded at a scan rate of 20 mV s^{-1} over a potential range of 0.7–1.70 V (*vs.* reversible hydrogen electrode, RHE). All measured potentials were calibrated to RHE using the Nernst equation:E(RHE) = E(SCE) + 0.244 V + 0.0591 pH (1). Double-layer capacitance (C_{dl}) was estimated in the non-faradaic region by measuring the capacitive current associated with double-layer charging, using CV scans at varying rates (20, 40, 60, 80, 100 mV s^{-1}). The long-term stability of the electrocatalysts was evaluated *via* chronopotentiometry at a constant current density of 50 mA cm^{-2} in 6 M KOH. EIS measurements for OER were conducted over a frequency range of 100 kHz to 1 Hz with an amplitude of 5 mV. The C_{dl} value was determined from the slope of a plot of $\Delta j/2$ (median current density at different scan rates) *versus* scan rate (abscissa). The electrochemical active surface area (ECSA) was calculated using the equation: ECSA = C_{dl}/C_s, where C_s (system-specific capacitance constant) was set to 0.04 mF cm^{-2}. Since C_{dl} is proportional to ECSA, it was used to compare electrocatalytic activity.

Turnover frequency (TOF) was employed as a direct descriptor of intrinsic catalytic activity, defined as the amount of product formed or reactant consumed per unit time per unit catalyst. For electrocatalytic OER, the most commonly used TOF equation is:

$$\mathrm{TOF} = (j \times A)/(n \times x \times F) \quad (1)$$

where j is the current density at a given overpotential, A is the electrode geometric area (1 cm^2), n is the number of electrons

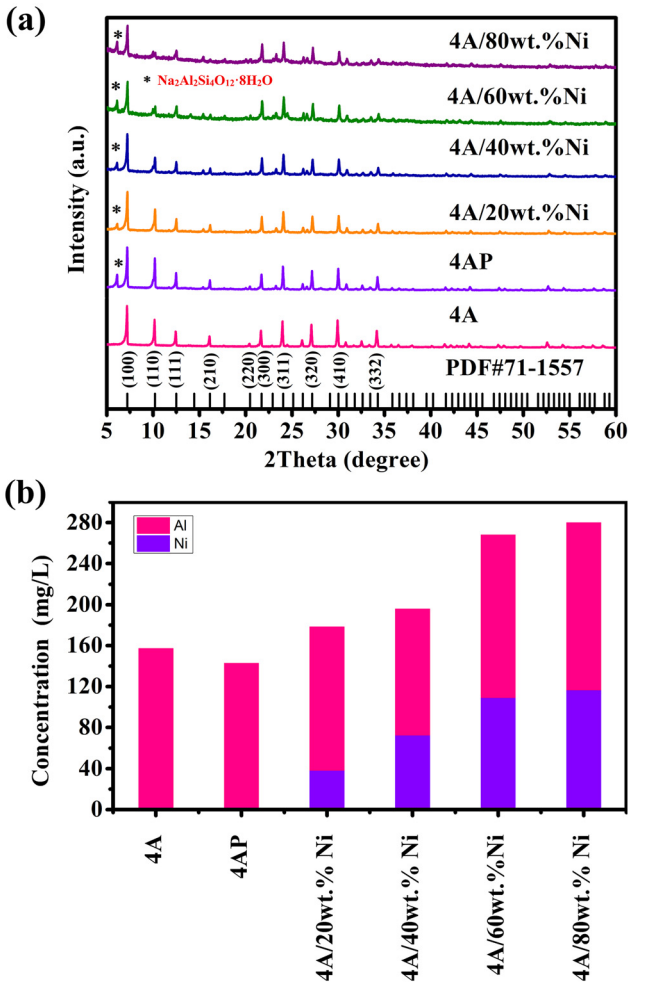

Fig. 1 (a) XRD patterns of all samples (4A, 4AP, and 4A/*x*Ni with x = 20, 40, 60, 80 wt%); (b) elemental content of all samples (4A, 4AP, and 4A/*x*Ni with x = 20, 40, 60, 80 wt%) determined by ICP analysis.

transferred (4 for OER), F is the Faraday constant, and x is the molar amount of catalytic active sites.

For Ni-based OER catalysts, the oxidation of Ni^{2+} to Ni^{3+} ($Ni^{2+} - e^- \rightarrow Ni^{3+}$) precedes water oxidation, with Ni^{3+} acting as the OER active site. Thus, the number of active sites (x) was determined by integrating the Ni^{2+}/Ni^{3+} redox charge (Q_{Redox}, peak area),[18,19] where z_2 (electron transfer number for metal electrocatalysis) = 1:

$$x = Q_{Redox} \times N_A/(z_2 \times F) \quad (2)$$

Substituting eqn (2) into eqn (1) gives the simplified TOF equation:

$$TOF = (j \times A)/(n \times x \times F) = I/(4 \times Q_{Redox}). \quad (3)$$

3 Results and discussion

3.1 XRD analysis

The XRD pattern of 4A zeolite is shown in Fig. S1. Sharp diffraction peaks were observed at 2θ = 7.2°, 10.2°, 12.5°, 16.1°, 20.5°, 21.7°, 24.0°, 27.2°, 29.1°, and 34.3°, corresponding to the (100), (110), (111), (210), (220), (300), (321), (400), and (332) planes of 4A zeolite ($Na_{12}Al_{12}Si_{12}O4_8$, PDF #71-1557), respectively.[20–22] As presented in Fig. 1a, the XRD patterns of all 4A/xNi (x = 20, 40, 60, 80 wt%) samples retained the characteristic peaks of 4A zeolite, confirming that the crystal structure of 4A zeolite was preserved in all samples. Additionally, a distinct diffraction peak at 2θ = 6.1° was observed, which can be attributed to $Na_2Al_2Si_4O_{12}{\cdot}8H_2O$ (PDF#39-1380). During the preparation of the 4AP sample, the etching effect of ammonia water caused the Si and Al species (derived from SiO_2 and Al_2O_3 components of 4A zeolite) to detach from the framework and enter the solution. The free Si and Al species in the solution reacted with Na^+ in the system (originating from Na^+ in 4A zeolite itself and NaOH added during the preparation process), eventually forming a composite oxide of $Na_2Al_2Si_4O_{12}{\cdot}8H_2O$. As the hydrothermal reaction proceeded and crystallization occurred, this composite oxide precipitated in an ordered crystal phase, manifesting as a characteristic diffraction peak at around 6.1° in the PXRD spectrum.

During the synthesis of 4A/xNi (x = 20, 40, 60, 80 wt%), the Al content decreased due to non-selective corrosion of Si and Al in the zeolite by ammonia, while the Ni content increased

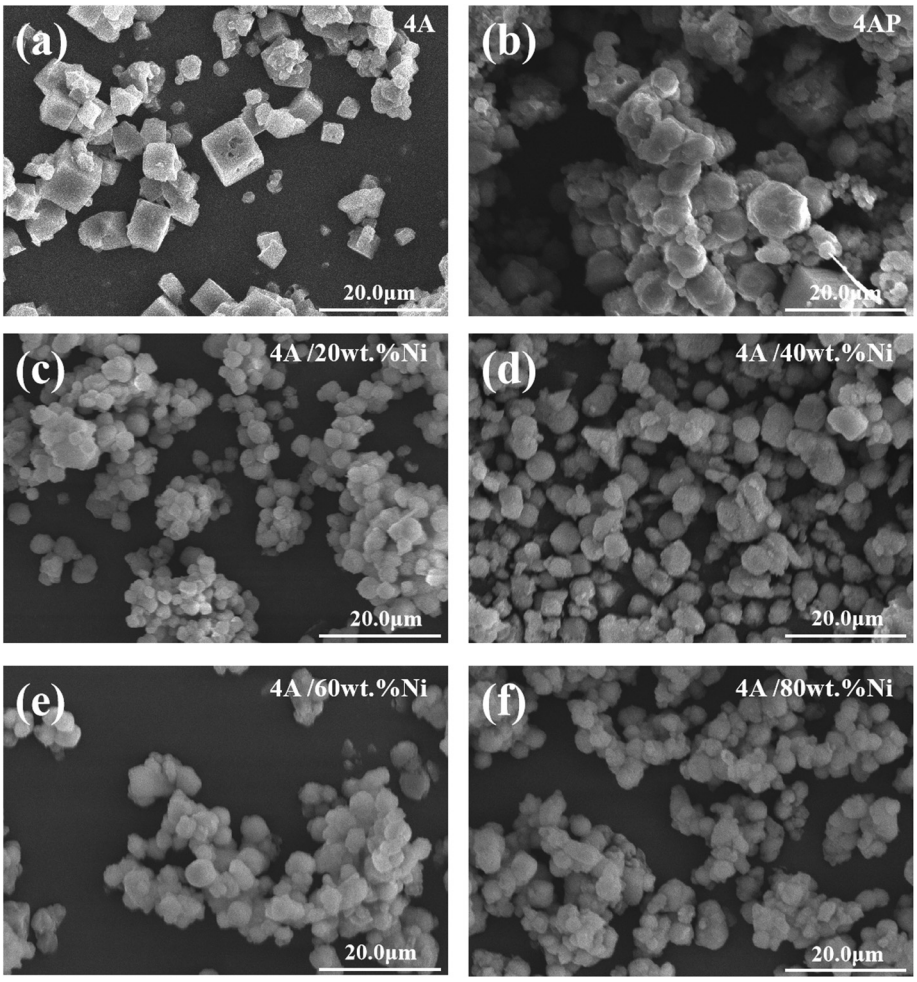

Fig. 2 (a–f) SEM images of all samples (4A, 4AP, and 4A/xNi with x = 20, 40, 60, 80 wt%).

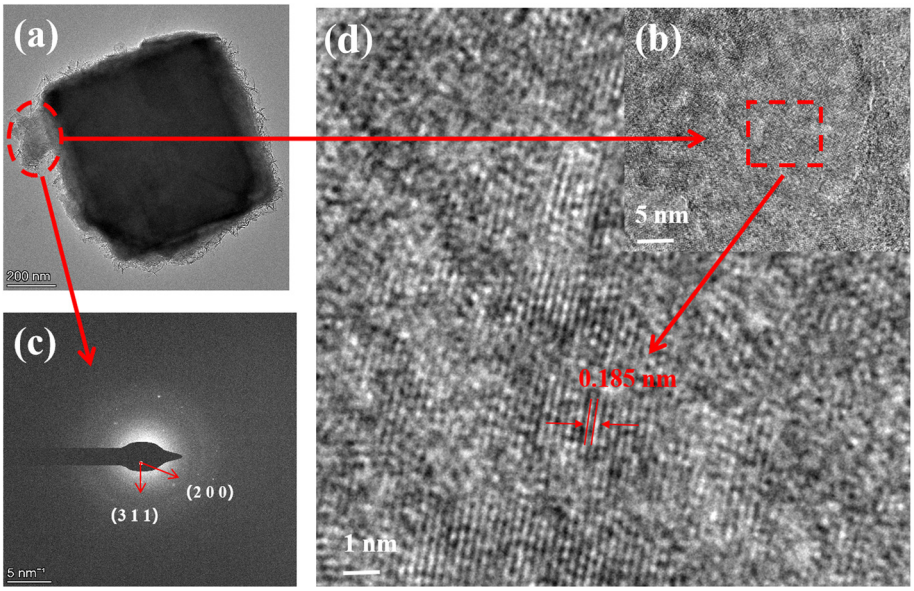

Fig. 3 (a) Transmission electron microscopy (TEM) images of 4A/80 wt% Ni, (b & d) HRTEM images of 4A/80 wt% Ni, (c) diffraction rings of 4A/80 wt% Ni.

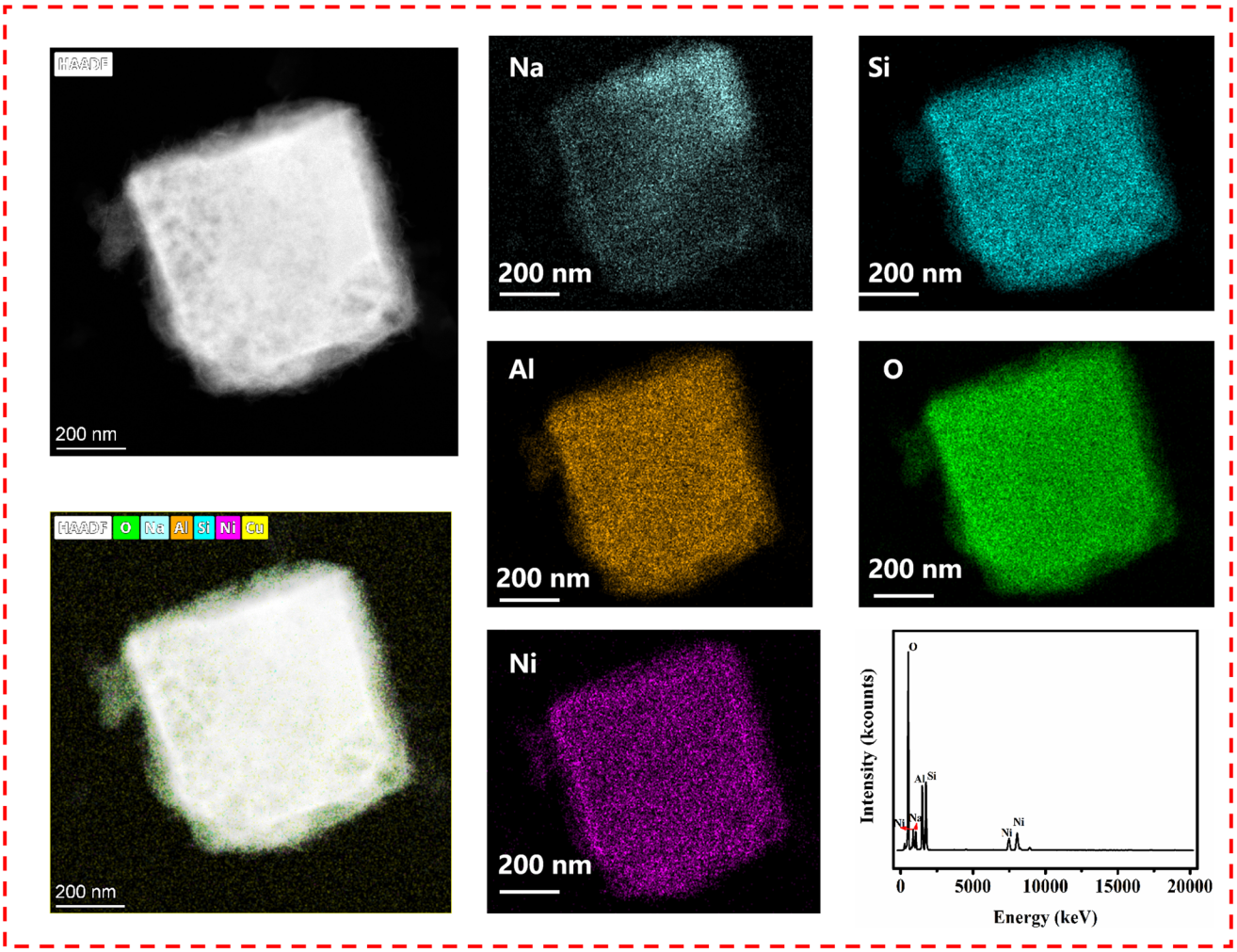

Fig. 4 High-angle annular dark-field (HAADF)-scanning transmission electron microscopy (STEM) imaging of 4A/80 wt% Ni sample and the corresponding elemental mappings of Na, Si, Al, O, and Ni.

gradually with the loading of $Ni(NO_3)_2{\cdot}6H_2O$, as shown in Fig. 1b and Table S1. EDX analysis (Fig. S2 and S3) confirmed that Al and Ni were successfully loaded onto 4A zeolite in 4A, 4AP, and 4A/*x*Ni samples. The presence of Ni^{2+} ions as charge-balancing cations in 4A promoted instability and hydrolysis of the zeolite framework. Specifically, most or all Ni^{2+} ions in hydrated 4A existed as the aqueous complex $[Ni(H_2O)_6]^{2+}$. They retained an aqueous coordination sphere without direct coordination to the anionic zeolite framework, unlike most other charge-balancing cations.[23] Notably, Ni loading did not destroy the 4A framework (Fig. 1a), which is favorable for maintaining structural stability during OER.

3.2 SEM analysis

The SEM images of all samples are shown in Fig. 2. The as-synthesized 4A zeolite (Fig. 2a) exhibited good dispersion, high crystallinity, and a cubic-like structure with a particle size of approximately 2 μm, consistent with the typical morphology of 4A zeolite.[24] After ammonia water treatment, the edges and corners of 4A zeolite were smoothened, transforming its shape from cubic to oval (Fig. 2b). The SEM images of 4A/*x*Ni samples with Ni loadings of 20, 40, 60, and 80 wt%, respectively, are shown in Fig. 2c–f. The prepared 4A/*x*Ni (*x* = 20, 40, 60, 80 wt%) samples evidently retained the crystal structure of 4A zeolite and maintained good crystallinity. Combined with XRD, SEM, and ICP analyses, these results confirm the successful synthesis of 4A/*x*Ni (*x* = 20, 40, 60, 80 wt%) composites.

To further investigate the structural features of 4A/80 wt% Ni, high-resolution transmission electron microscopy (HRTEM) and selected area electron diffraction (SAED) analyses were performed. Representative images of 4A/80 wt% Ni are presented in Fig. 3 and 4. High-magnification TEM images (Fig. 3a) revealed a typical cubic structure, consistent with the SEM observations (Fig. 2). HRTEM images (Fig. 3b and d) of 4A/80 wt% Ni showed a set of lattice fringes corresponding to NiO. The (310) and (200) planes of 4A zeolite and NiO observed in the SAED patterns (Fig. 3c) were highly consistent with those in the XRD pattern (Fig. 1).

3.3 BET analysis

The specific surface area and pore size data of all the samples are presented in Table S2. The specific surface area of pure 4A zeolite was 1.54 $m^2\ g^{-1}$, while 4AP and 4A/*x*Ni (*x* = 20, 40, 60, 80 wt%) composites exhibited significantly higher values. Notably, the specific surface area of 4A/*x*Ni samples increased with the rise in Ni content; 4A/80 wt% Ni exhibited the largest value of 46.63 $m^2\ g^{-1}$ (Table S2). In addition, 4AP and 4A/*x*Ni (*x* = 20, 40, 60, 80 wt%) displayed type IV adsorption–desorption isotherms and type H3 hysteresis loops (Fig. 5a and b), indicating the formation of mesopores in the 4A zeolite after alkali etching.

3.4 Electrochemical properties

To investigate the optimal OER performance of 4A samples doped with nickel ions at different mass ratios (*x*Ni = 20, 40, 60, 80 wt%), linear sweep voltammetry (LSV) was performed,

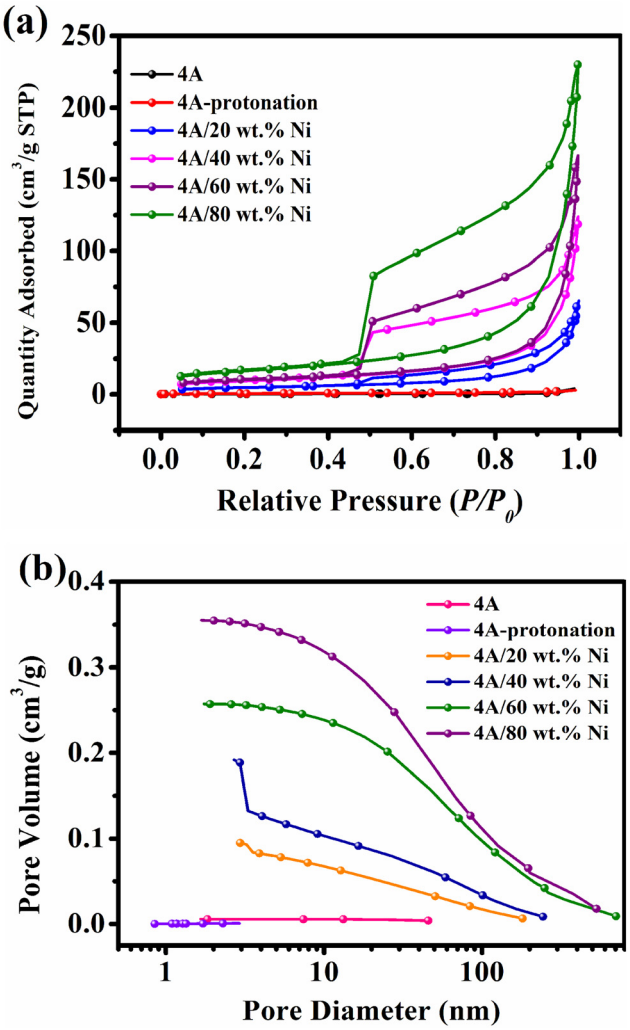

Fig. 5 N_2 adsorption/desorption isotherms (a) and pore size distribution (b) of 4A, 4AP and 4A/*x*Ni (*x* = 20, 40, 60, 80 wt%).

and the LSV curves of the samples are shown in Fig. 6a. At a current density of 10 mA cm^{-2}, the onset potential of 4A zeolite was 1.396 V, and that of 4AP was 1.395 V. The onset potentials of 4A/*x*Ni (*x* = 20, 40, 60, 80 wt%) were 1.406 V, 1.396 V, 1.389 V, and 1.422 V, respectively. The onset potentials of 4A/*x*Ni (*x* = 20, 40, 60 wt%) varied slightly, with 4A/60 wt% Ni exhibiting the lowest value. As shown in Fig. 6b, the Tafel slope of 4A/*x*Ni (*x* = 20, 40, 60, 80 wt%) decreased gradually with an increase in Ni content. The Tafel slope of 4A/80 wt% Ni was 19.0 mV dec^{-1}, which was lower than that of the 4A zeolite sample, indicating better catalytic activity. The electric double layer capacitance (C_{dl}) of 4A zeolite was 37.3 μF cm^{-2}, while 4A/60 wt% Ni exhibited the maximum C_{dl} of 98.3 μF cm^{-2} (Fig. 6c). This result suggests that 4A/60 wt% Ni possessed a greater number and density of active sites, expanding the electrochemical active region. 4A/60 wt% Ni showed the lowest onset potential and highest C_{dl}, indicating that moderate Ni loading balanced active site density and electron transfer efficiency. In Fig. 6d, the intercept of each Nyquist plot

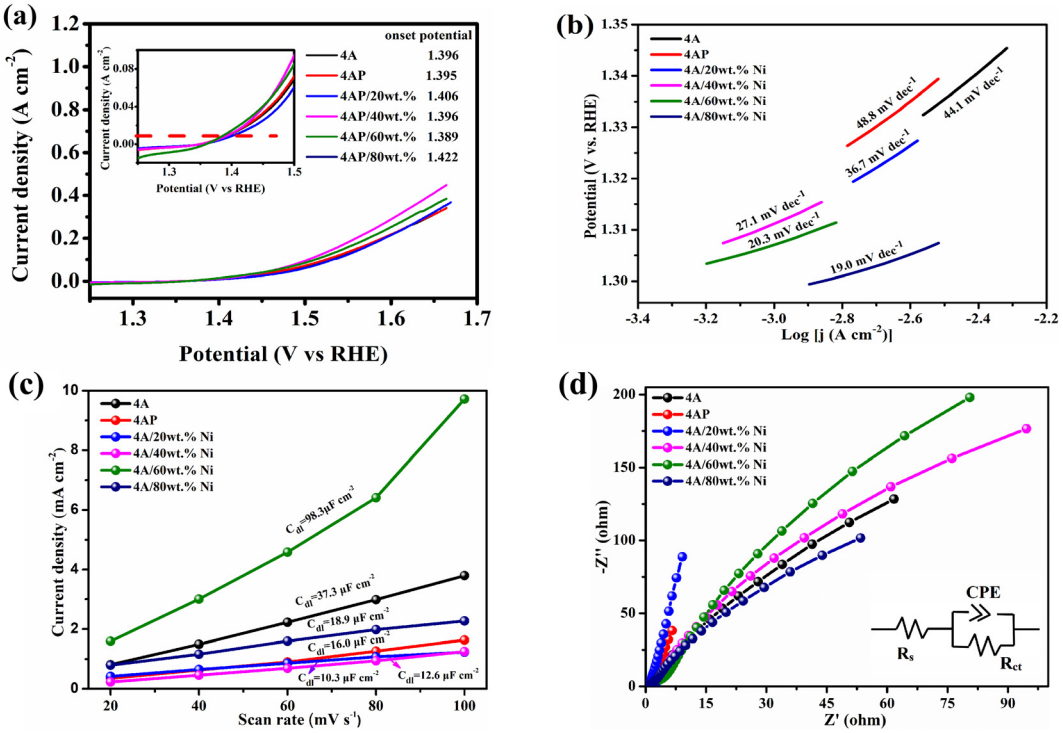

Fig. 6 (a) Linear sweep voltammetry (LSV) curves, (b) Tafel plots, (c) double-layer capacitance (C_{dl}) measurements, and (d) Nyquist plots of all tested samples (4A, 4AP, and 4A/xNi composites with x = 20, 40, 60, 80 wt%).

with the X-axis in the high-frequency region represents the intrinsic resistance (R_s), which reflects the combined influence of the active material and electrolyte ions. A smaller R_s indicates lower intrinsic resistance of the material, facilitating electron transport. The R_s values of 4A zeolite, 4AP, and 4A/xNi (x = 20, 40, 60, 80 wt%) were 185 Ω, 471 Ω, 630 Ω, 225 Ω, 315 Ω, and 157 Ω, respectively. A comparison of OER kinetic parameters of all the prepared samples and some related electrocatalysts from literature reports is presented in Table 2.

TOF is a reliable index to evaluate the intrinsic activity of a catalyst, applicable to electrocatalytic reactions involving both fuel generation and consumption. For Ni-based OER catalysts, the oxidation of Ni (electron loss) precedes water oxidation in OER: $Ni^{2+} - e^- \rightarrow Ni^{3+}$. These hypervalent Ni(III) species are recognized as OER active sites that initiate OER. Thus, the number of active sites can be determined by integrating the Ni^{2+}/Ni^{3+} redox charge (Q, peak area).[18,19] The TOF values of the four samples in this study were calculated using eqn (3), as shown in Fig. 7b and Table S3. Here, Q_{REDOX} (redox charge) in the TOF calculation was derived from the peak area of each sample in Fig. 7a. Evidently, 4A/80 wt% Ni exhibited the highest TOF (0.37 s^{-1}) among all samples, indicating its highest intrinsic activity.

SEM images (Fig. 2) showed that 4A/60 wt% Ni retained a cubic morphology with uniform Ni distribution, consistent with STEM elemental mapping results (Fig. 4). This confirmed homogeneous Ni loading, which contributed to the high electrochemical active surface area (ECSA) observed for 4A/60 wt% Ni (Fig. 7a). The stability of electrode materials is a critical factor in evaluating electrocatalytic performance. The 600 s chronopotentiometry (CP) curves of 4A/xNi (x = 20, 40, 60, 80 wt%) are displayed in Fig. 7c, and the 3 h CP curve of 4A/60 wt% Ni is presented in Fig. 7d. After 600 s and 3 h of testing at a current density of 50 mA cm^{-2}, the oxygen evolution potential of each sample remained relatively stable, demonstrating good electrochemical stability. The ECSA of 4A/60% Ni was much higher than that of 4A/80% Ni, and the initial potential was lower (1.389 V < 1.422 V), indicating a higher density of active sites. The pore volume of 4A/80% Ni was larger (Type IV isothermal line), but its activity was poor because the excessive Ni aggregates reduced the accessibility of the sites.

Table 2 Comparison of OER kinetic parameters of as-prepared samples and related electrocatalysts from literature reports

Samples	Electrolyte	$E_{onset/V}$	Tafel slope (mV dec^{-1})	Ref.
Comm NiO	1.0 M KOH	~1.52	92	25
Ce-ZSM-5		1.68	207	26
CoZIF-9(III) sheets		1.61	55	27
4A	6.0 M KOH	1.396	44.1	This work
4AP		1.395	48.8	
4A/20 wt% Ni		1.406	36.7	
4A/40 wt% Ni		1.396	27.1	
4A/60 wt% Ni		1.389	20.3	
4A/80 wt% Ni		1.422	19	

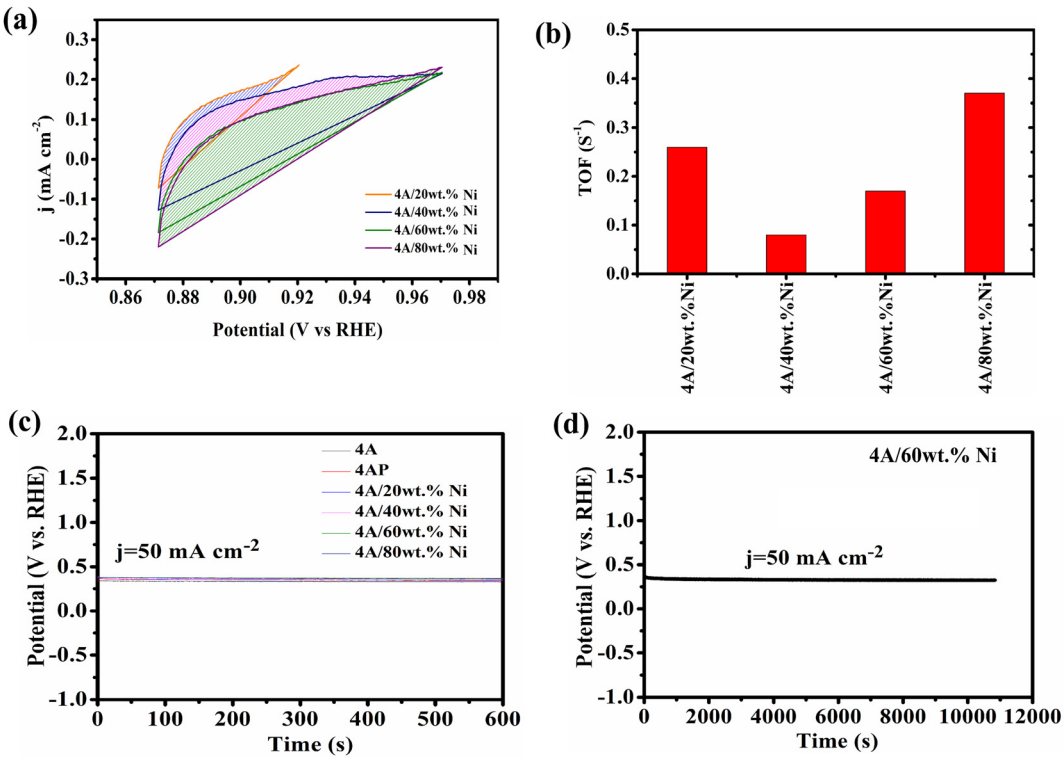

Fig. 7 (a) Isolated oxidation peaks of all the samples used for charge integration and calculation of the number of active sites, (b) specific activity and TOF determined using the calculated number of sites from the charge integrated from the oxidation peaks shown in (b),[18] (c) stability test conducted by chronopotentiometry technique (600 s) of 4A/*x*Ni (*x* = 20, 40, 60, 80 wt%) and (d) stability test conducted by chronopotentiometry technique (3 h) of 4A/60 wt% Ni.

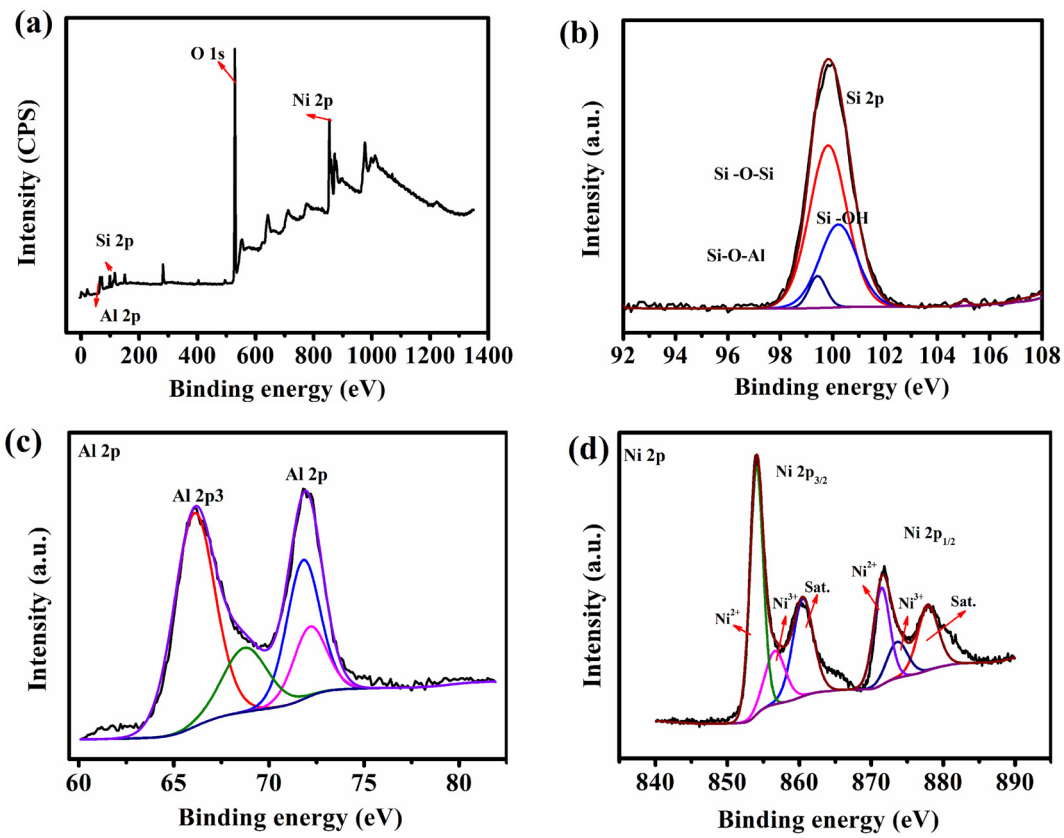

Fig. 8 XPS survey and wide scan spectra of 4A/60 wt% Ni. (a) Full spectrum, (b) Si 2p, (c) Al 2p, (d) Ni 2p.

3.5 XPS analysis

Comparing the XPS spectra in Fig. 8a, 4A/60 wt% Ni clearly exhibited signals corresponding to Al, Si, Ni, and O. The high-resolution Si 2p spectrum of 4A/60 wt% Ni can be deconvoluted into three fitted peaks (Fig. 8b), which are assigned to Si–O–Al (99.9 eV), Si–O–Si (100.3 eV), and Si–OH (99.5 eV) species. As shown in Fig. 8c, the Al 2p XPS spectrum of 4A/60 wt% Ni displayed two distinct peaks at 66–68.9 eV and 71.8–72.2 eV, attributed to Ni 3p[28] and Al 2p,[29,30] respectively.

The Ni 2p spectrum of 4A/60 wt% Ni is presented in Fig. 8d. Two spin-split doublets and two "Sat."-labeled satellite peaks were observed, indicating the coexistence of Ni^{2+} and Ni^{3+} oxidation states. The two major peaks of 4A/60 wt% Ni at 853.9 eV and 871.2 eV correspond to Ni $2p_{3/2}$ and Ni $2p_{1/2}$.[31] Additionally, the main peak of 4A/60 wt% Ni can be deconvoluted into two sub-peaks at 853.9 eV and 856.7 eV (first doublet), corresponding to the Ni^{2+} oxidation state in Ni $2p_{3/2}$ and Ni $2p_{1/2}$. The second doublet at 871.2 eV and 873.8 eV is assigned to the Ni^{3+} oxidation state in Ni $2p_{3/2}$ and Ni $2p_{1/2}$.[32] The two pairs of satellite peaks at 860.2 eV and 877.9 eV correspond to Ni $2p_{3/2}$ and Ni $2p_{1/2}$, indicating the presence of Ni $(OH)_2$ and Ni–O species on the surface.[33]

4. Conclusion

A series of 4A/*x*Ni (x = 20, 40, 60, 80 wt%) materials was successfully synthesized *via* a hydrothermal method. Among all samples, 4A/80 wt% Ni exhibited the largest specific surface area of 46.63 $m^2\ g^{-1}$. Notably, 4A/60 wt% Ni demonstrated optimal OER activity, characterized by a low onset potential (1.389 V), a small Tafel slope, and low resistance. This superior performance is attributed to its high electrochemical active surface area and uniform Ni distribution. Additionally, 4A/60 wt% Ni exhibited the largest capacitance density (98.3 $\mu F\ cm^{-2}$) among all samples. These results indicate that the as-prepared 4A/60 wt% Ni catalyst holds broad application prospects in OER. This work presents a scalable strategy for designing zeolite-supported transition metal catalysts and highlights the significance of tuning metal loading to balance surface area and active site density in OER applications.

Author contributions

Xiu-Zhen Xie and Chenglu Hu contributed equally to this work. Xiu-Zhen Xie: methodology, investigation, formal analysis, writing original draft, review & editing. Chenglu Hu: methodology, investigation, formal analysis, writing original draft, review & editing. Cao Luo: methodology, investigation, formal analysis. QiuJie Shi: methodology, investigation, formal analysis. Yongyang Wang: methodology, investigation, formal analysis. Qizhi Le: supervision, validation, review & editing. Wenyi Hu: supervision, validation, review & editing.

Conflicts of interest

The authors declare that they have no conflict of interest.

Data availability

The data supporting this article have been included as part of the supplementary information (SI). Supplementary information: synthetic protocol, XRD patterns; SEM, TEM, XPS, BET, HRTEM, ICP, FTIR, OER test. See DOI: https://doi.org/10.1039/d5dt02450a.

Acknowledgements

We acknowledge the funding supported from: (1) 2024 Fujian Province Young and Middle-aged Teachers Education Research Project (Science and Technology) (JZ240070); (2) Project of the Science and Technology Department of Fujian Province (2025J011020).

References

1 D. Farrusseng and A. Tuel, *New J. Chem.*, 2016, **40**, 3933–3949.
2 T. Iida, D. Zanchet, K. Ohara, T. Wakihara and Y. Román-Leshkov, *Angew. Chem., Int. Ed.*, 2018, **57**, 6454–6458.
3 M. A. Deimund, J. Labinger and M. E. Davis, *ACS Catal.*, 2014, **4**, 4189–4195.
4 Z. Zhang, Q. Xiao and J. Gu, *Dalton Trans.*, 2020, **49**, 14771–14775.
5 C. Zhao, Y. Wang, Z. Li, W. Chen, Q. Xu, D. He, D. Xi, Q. Zhang, T. Yuan, Y. Qu, J. Yang, F. Zhou, Z. Yang, X. Wang, J. Wang, J. Luo, Y. Li, H. Duan, Y. Wu and Y. Li, *Joule*, 2019, **3**, 584–594.
6 Z. Fan, Y. Ji, Q. Shao, S. Geng, W. Zhu, Y. Liu, F. Liao, Z. Hu, Y. C. Chang, C. W. Pao, Y. Li, Z. Kang and M. Shao, *Joule*, 2021, **5**, 3221–3234.
7 R. Ryoo, J. Kim, C. Jo, S. W. Han, J.-C. Kim, H. Park, J. Han, H. S. Shin and J. W. Shin, *Nature*, 2020, **585**, 221–224.
8 H. Peng, T. Dong, S. Yang, H. Chen, Z. Yang, W. Liu, C. He, P. Wu, J. Tian, Y. Peng, X. Chu, D. Wu, T. An, Y. Wang and S. Dai, *Nat. Commun.*, 2022, **13**, 295.
9 P. Sazama, D. Kaucky, J. Moravkova, R. Pilar, P. Klein, J. Pastvova, E. Tabor, S. Sklenak, I. Jakubec and L. Mokrzycki, *Appl. Catal., A*, 2017, **533**, 28–37.
10 B. Iwanschitz, L. Holzer, A. Mai and M. Schütze, *Solid State Ionics*, 2012, **211**, 69–73.
11 Z. H. L. Zhang, J. Huang, *et al.*, *J. Adv. Ceram.*, 2022, **11**, 1294–1306.
12 X. Wei, Y. Li, Z. Hua, L. Chen and J. Shi, *ChemCatChem*, 2020, **12**, 6285–6290.
13 K. Yuan, T. Tianzhen, *et al.*, *J. Adv. Ceram.*, 2022, **11**, 882–892.

14 B. Kaur, R. Srivastava and B. Satpati, *ACS Catal.*, 2016, **6**, 2654–2663.
15 J. Pérez-Ramírez, C. H. Christensen, K. Egeblad, C. H. Christensen and J. C. Groen, *Chem. Soc. Rev.*, 2008, **37**, 2530–2542.
16 X. Z. Xie, Y. M. Pan and J. X. Mi, *Chemosphere*, 2022, **309**, 136741.
17 X. Z. Xie, Y. Pan and J. X. Mi, *CrystEngComm*, 2024, **26**, 40–50.
18 S. Anantharaj, P. E. Karthik and S. Noda, *Angew. Chem., Int. Ed.*, 2021, **60**, 23051–23067.
19 S. Anantharaj and S. Kundu, *ACS Energy Lett.*, 2019, **4**, 1260–1264.
20 Q. Meng, H. Chen, J. Lin, Z. Lin and J. Sun, *J. Environ. Sci.*, 2017, **56**, 254–262.
21 A. M. Cardoso, M. B. Horn, L. S. Ferret, C. M. N. Azevedo and M. Pires, *J. Hazard. Mater.*, 2015, **287**, 69–77.
22 K. S. Hui and C. Y. H. Chao, *J. Hazard. Mater.*, 2006, **137**, 401–409.
23 R. W. Cheary and A. Coelho, *J. Appl. Crystallogr.*, 1992, **25**, 109e121.
24 J. Cao, Q. Sun, P. Wang, J. Shen and X. Dai, *J. Dispersion Sci. Technol.*, 2020, **43**, 517–525.
25 S. S. Selvasundarasekar, S. Mahendran, M. Subir, A. BaQais, M. A. Amin and S. Kundu, *Inorg. Chem.*, 2023, **62**, 6411–6420.
26 J. Milikić, S. Stojanović, L. Damjanović-Vasilić, R. Vasilić, L. Rakočević, S. Lazarević and B. Šljukić, *J. Electroanal. Chem.*, 2023, **944**, 117668.
27 K. Jayaramulu, J. Masa, D. M. Morales, O. Tomanec, V. Ranc, M. Petr, P. Wilde, Y. T. Chen, R. Zboril, W. Schuhmann and R. A. Fischer, *Adv. Sci.*, 2018, **5**, 1801029.
28 N. Ohtsu, M. Oku, T. Shishido and K. Wagatsuma, *Appl. Surf. Sci.*, 2007, **253**, 8713–8717.
29 Z. Yan, Z. Xu, J. Yu and M. Jaroniec, *Appl. Catal., B*, 2016, **199**, 458–465.
30 I. V. Plyuto, A. P. Shpak, J. Stoch, L. F. Sharanda, Y. V. Plyuto, I. V. Babich, M. Makkee and J. A. Moulijn, *Surf. Interface Anal.*, 2006, **38**, 917–921.
31 M. Zhang, Z. Chen, H. Xu and K. Yan, *ACS Catal.*, 2020, **10**, 5179–5189.
32 P. Li, Y. Kuang, Y. Li, G. Zhang, W. Liu and X. Sun, *Adv. Energy Mater.*, 2018, **8**, 1703341.
33 S. Y. Hao, C. Yu, B. Yang, Z. Li, Y. Hou, L. Lei and X. Zhang, *ACS Energy Lett.*, 2019, **4**, 952–959.